

Type-II Weyl Points in Three-Dimensional Cold Atom Optical Lattices

Yong Xu* and L.-M. Duan†

Department of Physics, University of Michigan, Ann Arbor, Michigan 48109, USA

Topological Lifshitz phase transition characterizes an abrupt change of the topology of the Fermi surface through a continuous deformation of parameters. Recently, Lifshitz transition has been predicted to separate two types of Weyl points: type-I and type-II (or called structured Weyl points), which has attracted considerable attention in various fields. Although recent experimental investigation has seen a rapid progress on type-II Weyl points, it still remains a significant challenge to observe their characteristic Lifshitz transition. Here, we propose a scheme to realize both type-I and type-II Weyl points in three-dimensional ultracold atomic gases by introducing an experimentally feasible configuration based on current spin-orbit coupling technology. In the resultant Hamiltonian, we find three degenerate points: two Weyl points carrying a Chern number -1 and a four-fold degenerate point carrying a Chern number 2 . Remarkably, by continuous tuning of a convenient experimental knob, all these degenerate points can transition from type-I to type-II, thereby providing an ideal platform to study different types of Weyl points and directly probe their Lifshitz phase transition.

PACS numbers: 03.75.Ss, 37.10.Jk, 03.65.Vf, 03.75.Lm

I. INTRODUCTION

Distinct from conventional phase transitions driven by spontaneous symmetry breaking, Lifshitz phase transition is driven by an abrupt change of the topology of the Fermi surface [1]. Recently, it has been predicted in three-dimensional (3D) condensed matter materials that type-I Weyl fermions (i.e., Weyl points) [2–5] can transition to type-II [6] (or called structured Weyl points [7]) through Lifshitz transition [6, 7]. Although type-I Weyl fermions [8] were initially predicted in particle physics, type-II Weyl fermions may not be allowed to exist there due to Lorentz symmetry, which is absent in condensed matter materials. Such Lifshitz transition is perceived as the change of a type-I Weyl point’s single point Fermi surface to a type-II’s open Fermi surface consisting of particle and hole pockets along with a touching point [6, 7]. While remarkable experimental and theoretical progress has been reported recently on type-II Weyl semimetals and their properties [6, 7, 9–25], it remains a significant challenge in solid-state materials to observe the characteristic Lifshitz phase transition between type-I and type-II Weyl points.

Ultracold atomic gases provide an ideal platform to observe the Lifshitz transition because of their high controllability. And recent experiments on one-dimensional and two-dimensional (2D) spin-orbit coupling [26–35] in ultracold atomic gases have further paved the way for discovering novel topological quantum states [36–38]. Although type-I and type-II Weyl points were proposed in quasiparticle spectra of spin-orbit coupled Fermi superfluids [7, 39–43], realization of such superfluids is still a big challenge with current experimental technol-

ogy [28, 29, 31, 32]. A more feasible experimental scheme is to realize Weyl points in the single-particle spectra without the need of low-temperature Fermi superfluids. While some proposals have been made concerning type-I Weyl points [44–48], the scheme to realize both type-I and type-II Weyl points and their Lifshitz transition in the single-particle spectra of cold atoms is still lacking and highly desired.

In this paper, we propose a novel 3D model to realize both type-I and type-II Weyl points in the single-particle spectra of cold atoms in 2D optical lattices. In this model, we find two Weyl points carrying a Chern number -1 and a four-fold degenerate point carrying a Chern number 2 , protected by 2D pseudo-time-reversal (2D-PTRS), 2D inversion (2D-IS), and combined rotational symmetries. By continuous tuning of a Zeeman field, all these degenerate points can experience the Lifshitz transition from type-I to type-II. Furthermore, we find a laser-atom coupling configuration to implement the model based on the current experimental technology that realizes the required spin-orbit coupling. Due to the controllability of the Zeeman field through continuous tuning of a convenient experimental knob, this system offers a unique opportunity to observe the characteristic topological Lifshitz quantum phase transition between type-I and type-II Weyl points.

II. MODEL HAMILTONIAN

We start by briefly reviewing the concept of type-I and type-II Weyl points that are described by an effective Hamiltonian $H_W = v_0 k_z + \sum_{\mu=x,y,z} v_\mu k_\mu \sigma_\mu$ [6, 7], where k_μ (σ_μ) denote momenta (Pauli matrices) and v_0, v_μ are real parameters. Its energy spectrum is given by $E_\pm(\mathbf{k}) = v_0 k_z \pm \sqrt{\sum_{\mu=x,y,z} v_\mu^2 k_\mu^2}$ with \pm labeling particle and hole bands. When $|v_0| < |v_z|$, the energy of the

*Electronic address: yongxuph@umich.edu

†Electronic address: lmduan@umich.edu

particle (hole) band is positive (negative), except at the touching point where the energy vanishes. This touching point is dubbed type-I Weyl point. When $|v_0| > |v_z|$, in certain regions, the energy goes negative for the particle band and positive for the hole band, leading to an open Fermi surface besides a touching point at $E_{\pm}(\mathbf{k} = 0) = 0$. This structure is dubbed type-II Weyl point.

To realize both type-I and type-II Weyl points with cold atoms, we consider the following Hamiltonian that describes atoms in 2D optical lattices

$$H' = \frac{\mathbf{p}^2}{2m} + \sum_{\nu=x,y} V_{\nu} \sin^2(k_{L\nu} r_{\nu}) + h_z \sigma_z + V_{SO}, \quad (1)$$

where $\mathbf{p} = -i\hbar\nabla$ is the momentum operator, m is the mass of atoms, V_{ν} ($\nu = x, y$) denote the strength of optical lattices with the period being $a_{\nu} = \pi/k_{L\nu}$ along the ν direction, h_z is the Zeeman field, σ_{ν} are Pauli matrices for spins, and V_{SO} is a laser-induced spin-orbit coupling term taking the form

$$V_{SO} = \Omega_{SO}(M_x + iM_y)e^{ik_{Lz}r_z} |\uparrow\rangle\langle\downarrow| + \text{H.c.} \quad (2)$$

with $M_x = \sin(k_{Lx}r_x)\cos(k_{Ly}r_y)$, $M_y = \sin(k_{Ly}r_y)\cos(k_{Lx}r_x)$, Ω_{SO} proportional to the laser strength, and $k_{L\nu}$ with $\nu = x, y, z$ determined by lasers' wave vector along the ν direction. Later, we will describe the laser configuration that directly realizes the Hamiltonian (1), in particular the spin-orbit coupling term V_{SO} . Employing a unitary transformation with $U = e^{-ik_{Lz}r_z/2} |\uparrow\rangle\langle\uparrow| + e^{ik_{Lz}r_z/2} |\downarrow\rangle\langle\downarrow|$ yields $H = UH'U^{-1}$ with

$$H = \frac{\hbar^2 k_z^2}{2m} + \tilde{h}_z \sigma_z + H_{2D}, \quad (3)$$

where $k_z = p_z/\hbar$, $\tilde{h}_z = \hbar^2 k_{Lz} k_z / (2m) + h_z$, and the 2D Hamiltonian H_{2D} in the (x, y) plane is expressed as

$$H_{2D} = \sum_{\nu=x,y} \left[\frac{p_{\nu}^2}{2m} + V_{\nu} \sin^2(k_{L\nu} r_{\nu}) \right] + [\Omega_{SO}(M_x + iM_y) |\uparrow\rangle\langle\downarrow| + \text{H.c.}] \quad (4)$$

To see how the Weyl points emerge in this model, we discretize H_{2D} and study its physics in the tight-binding model (see Appendix A for details of discretization). The tight-binding form of H can be written as [let us first neglect $\hbar^2 k_z^2 / (2m)$ term and focus on type-I Weyl points]

$$H_{TB} = \sum_{k_z} \sum_{\mathbf{x}} [\tilde{h}_z \hat{c}_{k_z, \mathbf{x}}^{\dagger} \sigma_z \hat{c}_{k_z, \mathbf{x}} + \sum_{\nu=x,y} (-t_{\nu} \hat{c}_{k_z, \mathbf{x}}^{\dagger} \hat{c}_{k_z, \mathbf{x} + \mathbf{g}_{\nu}} + (-1)^{j_x + j_y} t_{SO\nu} \hat{c}_{k_z, \mathbf{x}}^{\dagger} \sigma_{\nu} \hat{c}_{k_z, \mathbf{x} + \mathbf{g}_{\nu}} + \text{H.c.}], \quad (5)$$

where $\mathbf{g}_{\nu} = a_{\nu} \mathbf{e}_{\nu}$; $\hat{c}_{k_z, \mathbf{x}}^{\dagger} = (\hat{c}_{k_z, \mathbf{x}, \uparrow}^{\dagger} \hat{c}_{k_z, \mathbf{x}, \downarrow}^{\dagger})$ with $\hat{c}_{k_z, \mathbf{x}, \sigma}^{\dagger}$ ($\hat{c}_{k_z, \mathbf{x}, \sigma}$) being the creating (annihilating) operator and $\mathbf{x} = j_x a_x \mathbf{e}_x + j_y a_y \mathbf{e}_y$; t_{ν} and $t_{SO\nu}$ denote the tunneling and spin-orbit coupling strength along the ν direction.

Different from the well-known 2D Chern insulator [49, 50], this Hamiltonian involves the position

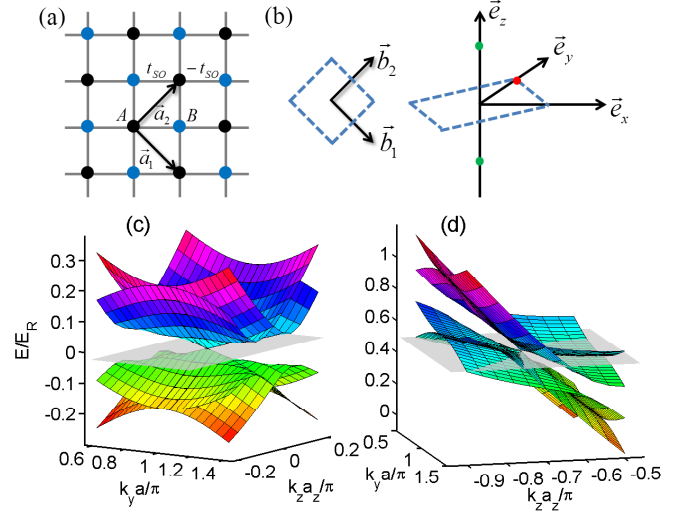


FIG. 1: (Color online) (a) Lattice structure in the (x, y) plane, where each unit cell is made up of A and B sites and $\mathbf{a}_1 = a\mathbf{e}_x - a\mathbf{e}_y$ with $a = a_x = a_y$ and $\mathbf{a}_2 = a\mathbf{e}_x + a\mathbf{e}_y$ are unit vectors. (b) The first Brillouin zone denoted by the dashed box. $\mathbf{b}_1 = \pi(\mathbf{e}_x - \mathbf{e}_y)/a$ and $\mathbf{b}_2 = \pi(\mathbf{e}_x + \mathbf{e}_y)/a$ are reciprocal unit vectors. Green $[\mathbf{k}^{W\pm} = (k_x^{W\pm}a, k_y^{W\pm}a, k_z^{W\pm}a_z) = (0, 0, 2m\pi(\pm 4t - h_z)/(\hbar^2 k_{Lz}^2))]$ and red solid $[\mathbf{k}^{W0} = (k_x^{W0}a, k_y^{W0}a, k_z^{W0}a_z) = (0, \pi, -2m\pi h_z/(\hbar^2 k_{Lz}^2))]$ circles denote the position where Weyl points exist in the momentum space. Here, $a_z = \pi/k_{Lz}$. (c)(d) Spectra near a type-I and type-II four-fold degenerate point with respect to $(k_x a, k_z a_z)$ for $k_x a = 0$ (see the spectra of the continuous model in Appendix A). In (d), the gray plane (i.e., $E = E_W$ with E_W being the energy at the degenerate point) intersects both the particle and hole bands in addition to the degenerate point, implying it is type-II. Here, $E_R = \hbar^2 k_R^2 / 2m$ with k_R being the absolute value of lasers' wave vector.

dependent spin-orbit coupling, and we thus need to choose a unit cell consisting of two sites: A and B [as shown in Fig. 1(a)] and the Hamiltonian in the momentum space in the new basis $\Psi(\mathbf{k})^T$ with $\Psi(\mathbf{k}) = (e^{ik_x a_x} \hat{A}_{\mathbf{k}\uparrow}, e^{ik_x a_x} \hat{A}_{\mathbf{k}\downarrow}, \hat{B}_{\mathbf{k}\uparrow}, \hat{B}_{\mathbf{k}\downarrow})$ reads

$$H_{TB}(\mathbf{k}) = \tilde{h}_z \sigma_z - h_t \tau_x + \tau_y (-d_x \sigma_x + d_y \sigma_y), \quad (6)$$

where $h_t = 2 \sum_{\nu=x,y} t_{\nu} \cos(k_{\nu} a_{\nu})$, $d_x = 2t_{SOx} \sin(k_x a_x)$ and $d_y = -2t_{SOy} \sin(k_y a_y)$; τ are Pauli matrices acting on A, B sublattices. In the (k_x, k_y) plane, $H_{TB}(\mathbf{k}_{\perp}, k_z)$ ($\mathbf{k}_{\perp} = k_x \mathbf{e}_x + k_y \mathbf{e}_y$) respects 2D-IS: $\tau_x H_{TB}(\mathbf{k}) \tau_x = H_{TB}(-\mathbf{k}_{\perp}, k_z)$ and when $\tilde{h}_z = 0$, 2D-PTRS: $\mathcal{T} H_{TB}(\mathbf{k}) \mathcal{T}^{-1} = H_{TB}(-\mathbf{k}_{\perp}, k_z)$ with $\mathcal{T} = i\tau_x \sigma_y \mathcal{K}$ and \mathcal{K} being the complex conjugate operator. These two symmetries guarantee that the spectrum in this specific plane ($\tilde{h}_z = 0$) is at least doubly degenerate, implying that the touching point, if exists, is four-fold degenerate. We note that in the continuous model 2D-IS corresponds to $\mathcal{I}_C H \mathcal{I}_C^{-1} = H(-r_x + \pi/k_{Lx}, -r_y, r_z) = H$ with the inversion center located at $(\pi/(2k_{Lx}), 0)$ and 2D-PTRS corresponds to $\mathcal{T}_C H_{2D} \mathcal{T}_C^{-1} = H_{2D}$ with $\mathcal{T}_C \equiv i\mathcal{I}_C \mathcal{P} \sigma_y \mathcal{K}$ and $\mathcal{P} H_{2D} \mathcal{P}^{-1} = H_{2D}(-r_x, -r_y)$.

Specifically, the eigenvalues of $H_{TB}(\mathbf{k})$ read $E_{\mathbf{k}} = \pm \sqrt{d_{\perp}^2 + (h_t \pm \tilde{h}_z)^2}$ with $d_{\perp}^2 = d_x^2 + d_y^2$, which supports the above symmetry analysis that the energy band at each \mathbf{k} is doubly degenerate without \tilde{h}_z . Clearly, when $d_x = d_y = 0$ and $h_t \pm \tilde{h}_z = 0$, there emerge degenerate points. This requires $(k_x a_x, k_y a_y) = (0, \pi)$ or $(0, 0)$. In the former case, a single degenerate point appears at $k_z^{W0} a_z = -2m\pi h_z / (\hbar^2 k_{Lz}^2)$ if $t_x = t_y$ (thus $h_t = 0$ at this point) as a result of a combined rotational symmetry (i.e., $U_4 H U_4^{-1} = H$ where $U_4 = S_4 C_4$ with $S_4 = e^{i\pi\sigma_z/4}$ and C_4 being the four-fold rotational operator along z when $V_x = V_y$ and $k_{Lx} = k_{Ly}$) readily achievable in experiments; in this plane, both 2D-PTRS and 2D-IS are preserved and this point's degeneracy is therefore four-fold (also seen from the eigenvalues). The dispersion is linear along all three momenta directions as visually shown in Fig. 1(c). Compared with a Dirac point in a Hamiltonian with both TRS and IS in 3D [50], in our case, two similar symmetries (2D-PTRS and 2D-IS) are both respected only in the plane $\tilde{h}_z = 0$. In fact, the four-fold degenerate point can be viewed as consisting of two Weyl points with the same Chern number. To demonstrate this, let us write down the effective Hamiltonian near the point, which, after a unitary transformation, reads

$$H(\mathbf{q}) \sim (v_z q_z \sigma_z + v_x q_x \sigma_x + v_y q_y \sigma_y) \tau_0, \quad (7)$$

where $v_z = \hbar^2 k_{Lz} / 2m$, $v_x = 2t_{SOx} a_x$, and $v_y = -2t_{SOy} a_y$; τ_0 is a 2×2 identity matrix; the momenta \mathbf{q} are measured with respect to the degenerate point. It is clear that each spinor corresponds to a Weyl point with the same chirality [51].

To characterize the topological charge of a degenerate point, we define the first Chern number

$$C = \frac{1}{2\pi} \sum_{n=1,2} \oint_{\mathcal{S}} \Omega_n(\mathbf{k}) \cdot d\mathcal{S}, \quad (8)$$

where the surface \mathcal{S} encloses a considered degenerate point, and $\Omega_n(\mathbf{k}) = i \langle \nabla_{\mathbf{k}} u_n(\mathbf{k}) | \times | \nabla_{\mathbf{k}} u_n(\mathbf{k}) \rangle$ is the Berry curvature [52] for the n -th band with $|u_n(\mathbf{k})\rangle$ being its wave function. For our parameters, a direct calculation yields $C = 2$ for the above discussed four-fold degenerate point.

In the latter case where $(k_x^{W\pm} a_x, k_y^{W\pm} a_y) = (0, 0)$, two degenerate points occur at $k_z^{W\pm} a_z = 2m\pi(\pm 4\bar{t} - h_z) / (\hbar^2 k_{Lz}^2)$ with $\bar{t} = (t_x + t_y) / 2$. Their degeneracy is double instead of four-fold (owing to the breaking of 2D-PTRS), and their dispersion is also linear in all three momentum directions. Our calculation demonstrates $C = -1$ for either of them. Due to the existence of the energy $\hbar^2 k_z^2 / (2m)$, the energy at these two Weyl points is different except when $h_z = 0$. Moreover, while we consider single-particle physics, a crude estimate using mean-field analysis suggests that weak repulsive short-range interactions may shift the locations of Weyl and four-fold degenerate points along z and cause the transition between the type-I and type-II but not destroy them (see Appendix B).

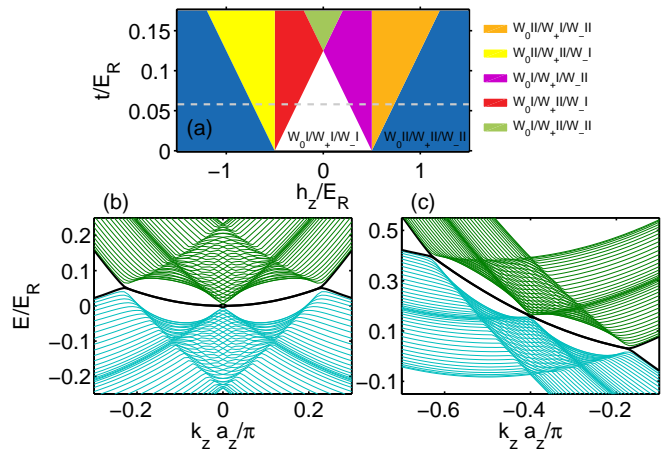


FIG. 2: (Color online) (a) Phase diagram with respect to h_z and t ($t = t_x = t_y$), in which $W_{\beta I}$ ($W_{\beta II}$) with $\beta = 0, +, -$ represent the phase with a type-I (type-II) Weyl or four-fold degenerate point located at $\mathbf{k}^{W\beta}$. The dashed line shows the case for $t = 0.058E_R$. (a)(b) Spectra as a function of $k_z a_z$ for $k_y = 0$ under open boundary condition along the x direction. In (a), $h_z = 0$ and the Weyl points are all type-I; in (b), $h_z = 0.4E_R$ and a Weyl point on the left side is type-II and all others are type-I. The black lines denote surface states.

To illustrate that these type-I Weyl and four-fold degenerate points can transition to type-II, we include $\hbar^2 k_z^2 / (2m)$ and expand the Hamiltonian near such points, e.g., $(0, \pi/a_y, k_z^{W0})$,

$$H(\mathbf{q}) \sim (v_0 q_z + v_z q_z \sigma_z + v_x q_x \sigma_x + v_y q_y \sigma_y) \tau_0 \quad (9)$$

with $v_0 = -2h_z/k_{Lz}$. Remarkably, when $|h_z| > \hbar^2 k_{Lz}^2 / (4m)$ (i.e., $|v_0| > v_z$), at certain regions, the energy of both particle bands goes negative while that of both hole bands goes positive [as visually displayed in Fig. 1(d)], indicating that the four-fold degenerate point becomes type-II. Similarly, the type-I Weyl point at \mathbf{k}^{W+} becomes type-II when $h_z < 4\bar{t} - \hbar^2 k_{Lz}^2 / (4m)$ or $h_z > 4\bar{t} + \hbar^2 k_{Lz}^2 / (4m)$, and the point at \mathbf{k}^{W-} becomes type-II when $h_z > -4\bar{t} + \hbar^2 k_{Lz}^2 / (4m)$ or $h_z < -4\bar{t} - \hbar^2 k_{Lz}^2 / (4m)$. In Fig. 2(a), we map out the phase diagram displaying the following phases: all degenerate points are type-I, all are type-II, and partial type-I and partial type-II. In cold atoms, h_z can be easily tuned by changing two-photon detuning to continuously drive the transition among different phases, thereby providing an ideal platform to directly observe the Lifshitz transition.

We now turn to the study of surface states in this system. In Fig. 2, the energy spectra with respect to $k_z a_z$ for $k_y = 0$ are plotted: (a) $h_z = 0$ with type-I degenerate points and (b) $h_z = 0.4E_R$ with a type-II point. It shows that in both cases there emerge surface states (called Fermi arc) connecting the four-fold degenerate point at the center with two other Weyl points on two sides. The spectra in Fig. 2(b) also illustrate the feature of the type-II Weyl point at $k_z a_z / \pi = -0.62$ that all the particle and hole bands near the point at each k_z are pos-

itive or negative with respect to E_{W-} , the energy at the point.

Apart from the model that we have discussed, if we choose a simplified scheme with $M_x = \sin(k_{Lx}r_x)e^{ik_{Ly}r_y}$ and $M_y = \sin(k_{Ly}r_y)e^{-ik_{Lx}r_x}$, we can still obtain both type-I and type-II Weyl points. However, while it still respects 2D-PTRS, it breaks 2D-IS, splitting the four-fold degenerate point into two doubly degenerate ones (see Appendix A). To satisfy these symmetry requirements, we need to add an additional term into the model (6) : $\tau_z(\alpha_1\sigma_y - \alpha_2\sigma_x)$ which respects 2D-PTRS but breaks 2D-IS. If $V_x = V_y$ and $k_{Lx} = k_{Ly}$, we have $\alpha_1 = \alpha_2 = \alpha$ due to a symmetry requirement (see Appendix A), and the spectrum is $E_{\mathbf{k}} = \pm\sqrt{(d_x + \lambda\alpha)^2 + (d_y - \lambda\alpha)^2 + (h_t - \lambda\tilde{h}_z)^2}$ with $\lambda = \pm 1$, and Weyl points occur at $[k_x^W a, k_y^W a, k_z^W a_z] = [\lambda\delta\theta, \pi + \lambda\delta\theta, -2m\pi h_z/(\hbar^2 k_{Lz}^2)]$ (or $[\lambda\delta\theta, -\lambda\delta\theta, 2m\pi(4\lambda\tilde{t}\cos\delta\theta - h_z)/(\hbar^2 k_{Lz}^2)]$) with $\delta\theta = -\sin^{-1}(\alpha/2t_{SOx})$. Moreover, when $|h_z| > \hbar^2 k_{Lz}^2/(4m)$ ($|h_z - 4\lambda\tilde{t}\cos\delta\theta| > \hbar^2 k_{Lz}^2/(4m)$), the former (latter) Weyl points become type-II.

III. REALIZATION OF TYPE-II WEYL POINTS

To realize the Hamiltonian (1), we propose an experimental scheme (as shown in Fig. 3) that is based on a modification of the experimental configuration in Ref. [33]. We consider two hyperfine states of alkali atoms such as ^{40}K and ^{87}Rb and employ two independent Raman processes to create the spin-dependent optical lattices. Each Raman process involves two linearly polarized blue-detuned Raman laser beams with the polarization being along y (parallel to the magnetic field) and x , respectively. Each pair of Raman laser beams is characterized by a pair of Rabi frequencies $[\Omega_1 = \Omega_{10} \sin(k_{Lx}r_x)e^{-ik_{Lz}r_z/2}, \Omega_2 = \Omega_{20} \cos(k_{Ly}r_y)e^{ik_{Lz}r_z/2}]$ and $[\Omega'_1 = \Omega_{10} \sin(k_{Ly}r_y)e^{-ik_{Lz}r_z/2}, \Omega'_2 = i\Omega_{20} \cos(k_{Lx}r_x)e^{ik_{Lz}r_z/2}]$, respectively. They form a standing wave along x or y but remain a plane wave along z . Since the laser beam Ω'_1 (Ω'_2) is obtained by reflecting the beam Ω_1 (Ω_2) by mirrors, they possess the same frequency ω_1 (ω_2), and no phase locking is required [53, 54]. The laser beam Ω_2 with a different frequency ω_2 is generated by applying an acoustic-optical modulator on a beam split from the first laser beam. Each pair of Raman laser beams couple two hyperfine states independently, leading to the spin-orbit coupling term V_{SO} with $\Omega_{SO} = \Omega_{10}^* \Omega_{20}/\Delta_e$. Moreover, owing to the Stark effects, these lasers also create optical lattices along the x and y directions: $V_x \sin^2(k_{Lx}r_x)$ and $V_y \sin^2(k_{Ly}r_y)$ with $V_x = V_y = 2(|\Omega_{10}|^2 - |\Omega_{20}|^2)/\Delta_e$. The Zeeman field h_z is generated by the two-photon detuning δ through $h_z = \delta/2$ as shown in Fig. 3. In comparison, a similar laser configuration can also realize the simplified spin-orbit coupling scheme that we mentioned before. In this case, we further simplify the

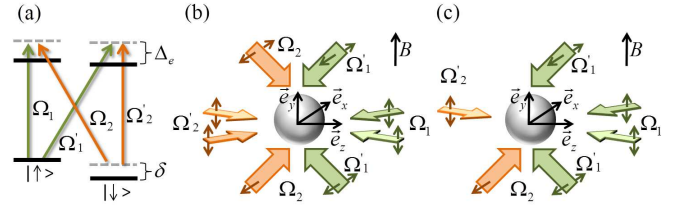


FIG. 3: (Color online) Schematics of laser configurations to realize the Hamiltonian (1) [(b)] and its simplified one [(c)]. Ω_1 (Ω_2) possess the same frequency as Ω'_1 (Ω'_2) generated by reflecting the laser beam Ω_1 (Ω_2) by mirrors. The magnetic field is along the y direction, and δ is the two-photon detuning. The double arrows denote the orientation of linear polarization of laser beams.

laser configuration [as shown in Fig. 3(c)] so that the Rabi frequencies take the form $\Omega_2 = \Omega_{20}e^{ik_{Lz}r_z/2 + ik_{Ly}r_y}$ and $\Omega'_2 = i\Omega_{20}e^{ik_{Lz}r_z/2 - ik_{Lx}r_x}$, corresponding to plane waves for the second set of laser beams.

We may choose either ^{40}K (fermions) or ^{87}Rb (bosons) atoms for observation of Weyl points in experiments. Here we take ^{40}K as an example. With a blue-detuned laser beam at wavelength 764 nm (corresponding to $\Delta_e = 2\pi \times 1.38$ THz) [28], the recoil energy $E_R/\hbar = 2\pi \times 8.5$ kHz. If we choose a geometry with $k_{Lx} = k_{Ly} = k_R \sin\theta$ and $k_{Lz} = 2k_R \cos\theta$ with $\theta = 60^\circ$ (the angle between laser beams and z axis), $\Omega_{10} = 2\pi \times 0.15$ GHz, $\Omega_{20} = \Omega_{10}/3$, we have $V_x = V_y = 3.7E_R$ and $\Omega_{SO} = 0.7E_R$. With these experimental parameters, the tight-binding parameters are $t_x = t_y = 0.058E_R$, and $t_{SOx} = -t_{SOy} = 0.028E_R$. δ can be readily tuned from zero and when δ crosses $0.53E_R$, we will observe a Lifshitz-type quantum phase transition from type-I to type-II Weyl points.

To detect the Weyl points of fermionic atoms and their Lifshitz phase transition, one can measure their linear spectra along all three momenta directions by momentum resolved radio-frequency spectroscopy, which has been utilized for observation of a 2D Dirac cone in spin-orbit-coupled atomic gases [31, 32]. The Lifshitz transition is directly reflected by a sharp change of the dispersion of particle or hole bands along k_z near a Weyl point so that the slopes of their spectra have the same sign. For bosonic atoms such as ^{87}Rb , although the Fermi surface does not exist, there is still the band structure with a touching point. One may consider driving a BEC across a Weyl point by a constant force F and measuring the Landau-Zener tunneling probability [48, 55–57], which is $P_{LZ} = e^{-\pi E_g^2/(4vF)}$ with E_g being the gap between the considered particle and hole bands and v being the velocity of the BEC [58]. Therefore, the gap closing at a Weyl point is signalled by a peak of the Landau-Zener tunneling probability. When the BEC bypasses a type-I (type-II) Weyl point, a finite fraction of atoms remains in the hole band and these atoms move in the opposite (same) direction along z compared with those tunneling into a higher band. This different behavior can be uti-

lized to measure the Lifshitz transition.

In summary, we have proposed a scheme well based on the current experimental technology to realize both type-I and type-II Weyl points in the single-particle spectra with cold atoms in an optical lattice. The proposed system offers a unique opportunity to observe and study the topological Lifshitz-type quantum phase transition from type-I to type-II Weyl points by continuously tuning one of the experimental knobs.

Acknowledgments

We thank S.-T. Wang and S. A. Yang for helpful discussions. This work was supported by the ARL, the IARPA LogiQ program, and the AFOSR MURI program.

Appendix A: DERIVATION OF TIGHT-BINDING MODEL

In this appendix, we derive the tight-binding model from the continuous model H in Eq. (3) in the main text and compare their spectra to verify the tight-binding model's reliability.

Let us first focus on the discretization of H_{2D} , which can be written as in the second quantization language

$$H_{II} = \int d\mathbf{r} \hat{\psi}^\dagger(\mathbf{r}) H_{2D} \hat{\psi}(\mathbf{r}), \quad (\text{A1})$$

where \mathbf{r} is restricted to the (x, y) plane and $\hat{\psi}(\mathbf{r}) = [\hat{\psi}_\uparrow(\mathbf{r}) \ \hat{\psi}_\downarrow(\mathbf{r})]^T$ with $\hat{\psi}_\sigma(\mathbf{r})$ [$\hat{\psi}_\sigma^\dagger(\mathbf{r})$] annihilating (creating) an atom with spin σ ($\sigma = \uparrow, \downarrow$) located at \mathbf{r} . They satisfy the anti-commutation or commutation relation $[\hat{\psi}_\sigma(\mathbf{r}), \hat{\psi}_{\sigma'}^\dagger(\mathbf{r}')]_{\pm} = \delta_{\sigma\sigma'} \delta(\mathbf{r} - \mathbf{r}')$ for fermionic atoms (+)

or bosonic atoms ($-$), respectively. We expand the field operator using local Wannier functions

$$\hat{\psi}_\sigma(\mathbf{r}) = \sum_{n, j_x, j_y, \sigma} W_{n, j_x, j_y} \hat{c}_{n, j_x, j_y, \sigma}, \quad (\text{A2})$$

where W_{n, j_x, j_y} is the Wannier function for $\Omega_{SO} = 0$ located at the site (j_x, j_y) for the n -th band, and $\hat{c}_{n, j_x, j_y, \sigma}$ ($\hat{c}_{n, j_x, j_y, \sigma}^\dagger$) annihilates (creates) an atom located at the state W_{n, j_x, j_y} with spin σ . Let us focus on the physics in the lowest band and thus assume $n = 1$, thereby simplifying the above expression

$$\hat{\psi}_\sigma(\mathbf{r}) \approx \sum_{j_x, j_y} W_{j_x, j_y} \hat{c}_{j_x, j_y, \sigma}, \quad (\text{A3})$$

where $W_j = W_{j_x}^x(r_x) W_{j_y}^y(r_y)$ with $W_{j_\nu}^\nu(r_\nu) = W^\nu(r_\nu - j_\nu a_\nu)$ being the Wannier function along ν . We note that although this is an approximation, it proves to be qualitatively correct and we will verify it by comparing the spectra obtained by solving the continuous model and the tight-binding one. Using this expansion, we obtain the following tight-binding model without V_{SO}

$$H_t = - \sum_{j_x, j_y, \sigma} \left(t_x \hat{c}_{j_x, j_y, \sigma}^\dagger \hat{c}_{j_x+1, j_y, \sigma} + t_y \hat{c}_{j_x, j_y, \sigma}^\dagger \hat{c}_{j_x, j_y+1, \sigma} \right) + \text{H.c.}, \quad (\text{A4})$$

where t_ν with $\nu = x, y$ denote the hopping amplitudes defined as

$$t_\nu = - \int dr_\nu W_{j_\nu}^\nu \left[\frac{p_\nu^2}{2m} + V_\nu \sin^2(k_{L\nu} r_\nu) \right] W_{j_\nu+1}^\nu. \quad (\text{A5})$$

We approximately derive the tight-binding term contributed by the spin-dependent lattice as follows

$$\begin{aligned} H_{SO} &= \Omega_{SO} \int d\mathbf{r} \hat{\psi}_\uparrow^\dagger(\mathbf{r}) (M_x + iM_y) \hat{\psi}_\downarrow(\mathbf{r}) + \text{H.c.}, \\ &\approx \Omega_{SO} \sum_{j_x, j_y} \sum_{j'_x, j'_y} \left[\hat{c}_{j_x, j_y, \uparrow}^\dagger \hat{c}_{j'_x, j'_y, \downarrow} t_{SOx}^{(j_x, j_y), (j'_x, j'_y)} - i \hat{c}_{j_x, j_y, \uparrow}^\dagger \hat{c}_{j'_x, j'_y, \downarrow} t_{SOy}^{(j_x, j_y), (j'_x, j'_y)} \right] + \text{H.c.}, \end{aligned} \quad (\text{A6})$$

where

$$t_{SOx}^{(j_x, j_y), (j'_x, j'_y)} = \int d\mathbf{r} W_{j_x, j_y} \sin(k_{Lx} r_x) \cos(k_{Ly} r_y) W_{j'_x, j'_y}, \quad (\text{A7})$$

$$t_{SOy}^{(j_x, j_y), (j'_x, j'_y)} = - \int d\mathbf{r} W_{j_x, j_y} \cos(k_{Lx} r_x) \sin(k_{Ly} r_y) W_{j'_x, j'_y}. \quad (\text{A8})$$

Note that we have added a minus sign in the definition of t_{SOy} in order to write the Hamiltonian in a compact form.

Employing the condition $W_0^\nu(r_\nu) = W_0^\nu(-r_\nu)$ given that one of the optical wells is located at $\mathbf{r} = (0, 0)$ when

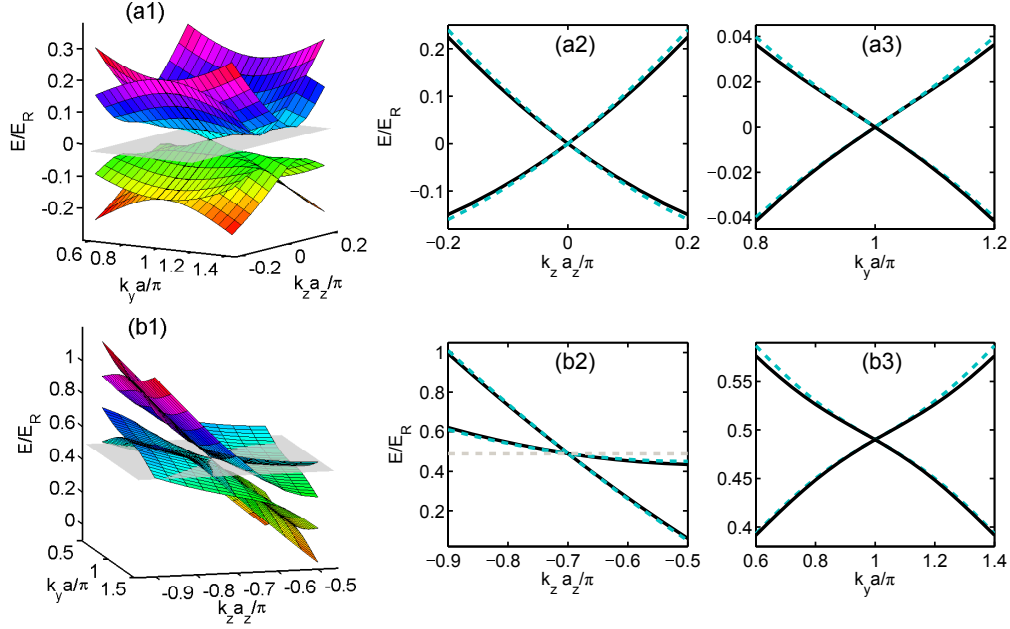


FIG. 4: (Color online) Single-particle spectra in the (k_y, k_z) plane for $k_x = 0$ obtained by ab initio theory (i.e., diagonalizing the continuous model) in (a1) and (b1) [the spectra of tight-binding model are plotted in Fig. 1(c) and (d) in the main text]. To compare these spectra in detail, we further plot them (with solid black and dashed cyan lines denoting the spectra of continuous and tight-binding model, respectively) around a degenerate point [$(k_y a/\pi = 1, k_z = 0)$ for the first row panel and $(k_y a/\pi = 1, k_z a_z/\pi = -0.7)$ for the second row panel] as a function of k_z and k_y in (a2,b2) and (a3,b3), respectively. Here, we choose $V_x = V_y = 3.7E_R$ and $\Omega_{SO} = 0.7E_R$ corresponding to the tight-binding model with $t_x = t_y = 0.058E_{R_x}$ and $t_{SO} = 0.028E_R$. For (a1-a3), $h_z = 0$, while for (b1-b3), $h_z = 0.7E_R$. For the spectra of the continuous model, we have shifted the energy at the degenerate point to the energy at the same point of the spectra of the tight-binding model.

$\Omega_{SO} = 0$, we get

$$t_{SOx}^{(j_x, j_y), (j_x, j'_y)} = t_{SOy}^{(j_x, j_y), (j'_x, j_y)} = 0, \quad (\text{A9})$$

$$t_{SOx}^{(j_x, j_y), (j_x+1, j_y)} = -t_{SOx}^{(j_x, j_y), (j_x-1, j_y)} = (-1)^{j_x+j_y} t_{SOx}^{(0,0), (1,0)}, \quad (\text{A10})$$

$$t_{SOy}^{(j_x, j_y), (j_x, j_y+1)} = -t_{SOy}^{(j_x, j_y), (j_x, j_y-1)} = (-1)^{j_x+j_y} t_{SOy}^{(0,0), (0,1)}, \quad (\text{A11})$$

where the last two relations are obtained because $\sin(k_{L\nu}(r_\nu + a_\nu)) = -\sin(k_{L\nu}r_\nu)$ and $\cos(k_{L\nu}(r_\nu + a_\nu)) = -\cos(k_{L\nu}r_\nu)$. Therefore, if we only consider the nearest-neighbor hopping, we obtain the following spin-orbit coupling term of the tight-binding model:

$$H_{SO} \approx \Omega_{SO} \sum_{j_x, j_y} \left(\hat{c}_{j_x, j_y, \uparrow}^\dagger \hat{c}_{j_x+1, j_y, \downarrow} t_{SOx}^{(j_x, j_y), (j_x+1, j_y)} + \hat{c}_{j_x, j_y, \uparrow}^\dagger \hat{c}_{j_x-1, j_y, \downarrow} t_{SOx}^{(j_x, j_y), (j_x-1, j_y)} - i \hat{c}_{j_x, j_y, \uparrow}^\dagger \hat{c}_{j_x, j_y+1, \downarrow} t_{SOy}^{(j_x, j_y), (j_x, j_y+1)} - i \hat{c}_{j_x, j_y, \uparrow}^\dagger \hat{c}_{j_x, j_y-1, \downarrow} t_{SOy}^{(j_x, j_y), (j_x, j_y-1)} \right) + \text{H.c.}, \quad (\text{A12})$$

$$= \Omega_{SO} \sum_{j_x, j_y} (-1)^{j_x+j_y} \left[t_{SOx}^{(0,0), (1,0)} (\hat{c}_{j_x, j_y, \uparrow}^\dagger \hat{c}_{j_x+1, j_y, \downarrow} - \hat{c}_{j_x, j_y, \uparrow}^\dagger \hat{c}_{j_x-1, j_y, \downarrow}) - i t_{SOy}^{(0,0), (0,1)} (\hat{c}_{j_x, j_y, \uparrow}^\dagger \hat{c}_{j_x, j_y+1, \downarrow} - \hat{c}_{j_x, j_y, \uparrow}^\dagger \hat{c}_{j_x, j_y-1, \downarrow}) \right] + \text{H.c.}, \quad (\text{A13})$$

$$= \sum_{\mathbf{x}} \sum_{\nu=x, y} (-1)^{j_x+j_y} t_{SO\nu} \hat{c}_{\mathbf{x}}^\dagger \sigma_\nu \hat{c}_{\mathbf{x}+\mathbf{g}_\nu} + \text{H.c.}, \quad (\text{A14})$$

where in the last step we have recast the Hamiltonian into a compact form by defining $t_{SO\nu} = \Omega_{SO} t_{SO\nu}^{(0,0), (0,1)}$, $\mathbf{g}_\nu = a_\nu \mathbf{e}_\nu$, $\hat{c}_{\mathbf{x}}^\dagger = (\hat{c}_{\mathbf{x}, \uparrow}^\dagger, \hat{c}_{\mathbf{x}, \downarrow}^\dagger)$ with $\hat{c}_{\mathbf{x}, \sigma}^\dagger \equiv \hat{c}_{j_x, j_y, \sigma}^\dagger$ and $\mathbf{x} = j_x a_x \mathbf{e}_x + j_y a_y \mathbf{e}_y$. When $V_x = V_y$ and $k_{Lx} = k_{Ly}$, $t_{SOx} = -t_{SOy}$. In 3D, after replacing $\hat{c}_{\mathbf{x}, \sigma}$ with $\hat{c}_{\mathbf{k}_z, \mathbf{x}, \sigma}$ and including H_t and the Zeeman field term, we obtain H_{TB} in Eq.(5) in the main text.

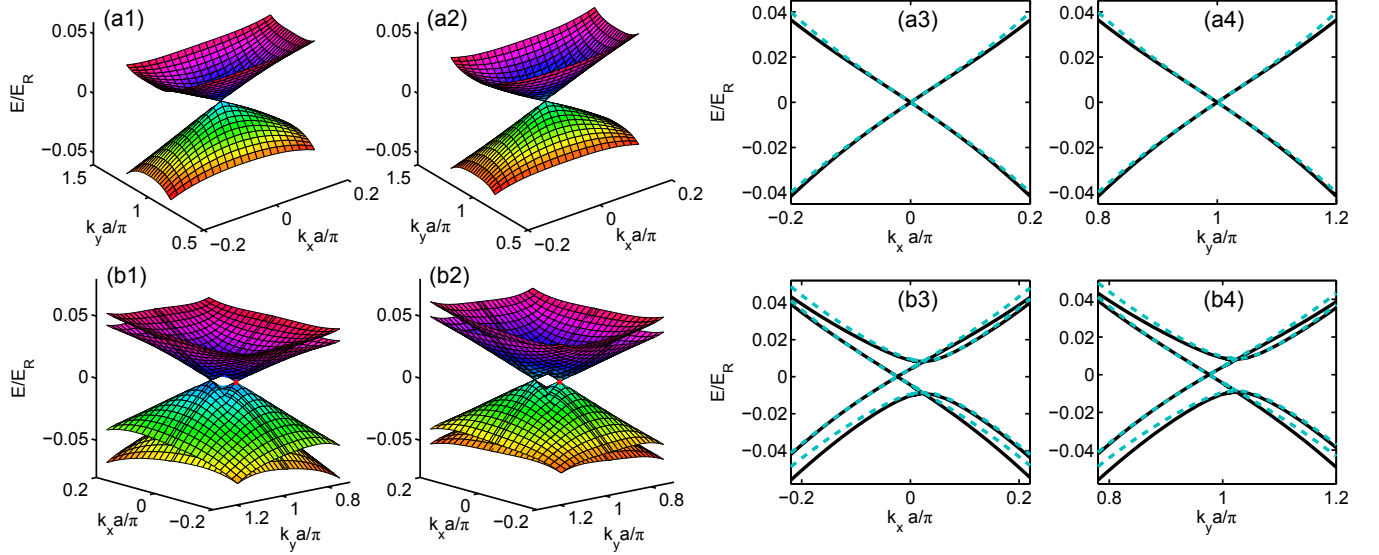


FIG. 5: (Color online) Single-particle spectra in the (k_x, k_y) plane for $k_z = 0$, obtained by ab initio theory in (a1) and (b1) and by diagonalizing the tight-binding model in (a2) and (b2). (a1-a4) correspond to the model with $M_x = \sin(k_{Lx}r_x) \cos(k_{Ly}r_y)$, $M_y = \sin(k_{Ly}r_y) \cos(k_{Lx}r_x)$, and (b1-b4) to the simplified model with $M_x = \sin(k_{Lx}r_x)e^{ik_{Ly}r_y}$ and $M_y = \sin(k_{Ly}r_y)e^{-ik_{Lx}r_x}$. To compare these spectra in detail, we further plot them (with solid black and dashed cyan lines denoting the spectra of continuous and tight-binding model, respectively) around a degenerate point $[(k_x = 0, k_y a/\pi = 1)$ for the first row panel and $(k_x a/\pi = -0.024, k_y a/\pi = 0.976)$ denoted by the red square in (b1) and (b2) for the second row panel] as a function of k_x and k_y in (a3,b3) and (a4,b4), respectively. Here, we choose $V_x = V_y = 3.7E_R$, $\Omega_{SO} = 0.7E_R$, and $h_z = 0$, corresponding to the tight-binding model with $t_x = t_y = 0.058E_{R_x}$ and $t_{SO} = 0.028E_R$. For comparison, we have shifted the spectra of the continuous model so that the energy at the degenerate point is zero.

To verify the reliability of the tight-binding model, in Fig. 4 and Fig. 5, we compare the energy spectra of the tight-binding model with those of the continuous model, which are numerically calculated using Fourier series expansion of a Bloch function. In Fig. 4 (a1) and (b1), we present the spectra of the continuous model, which qualitatively agree with their tight-binding counterparts in Fig. 1(c) and (d) of the main text. To see their difference more quantitatively, we plot their spectra around a degenerate point with respect to k_z and k_y in Fig. 4(a2,b2) and (a3,b3), respectively, illustrating excellent agreement between these two approaches in the vicinity of a degenerate point; this implies that the tight-binding model can well characterize these degenerate points. As momenta move far away from these points, there appears a slight discrepancy, which might be reduced when the next-nearest-neighbor hopping is included. In Fig. 5(a1-a2), we further compare their spectra in the (k_x, k_y) plane; the doubly degenerate spectra in Fig. 5(a) and those in Fig. 5(b) are in qualitative agreement with each other and both exhibit a four-fold degenerate point. In addition, a more quantitative comparison in Fig. 5(a3) and (a4) demonstrates the reliability of the tight-binding model.

For the simplified model with $M_x = \sin(k_{Lx}r_x)e^{ik_{Ly}r_y}$ and $M_y = \sin(k_{Ly}r_y)e^{-ik_{Lx}r_x}$, it breaks 2D-IS but still respects 2D-PTRS and therefore in the tight-binding model we need to add an additional term $\tau_z(\alpha_1\sigma_y - \alpha_2\sigma_x)$

that preserves 2D-PTRS but lacks 2D-IS. When $V_x = V_y$ and $k_{Lx} = k_{Ly}$, we have $\alpha_1 = \alpha_2 = \alpha$ because the 2D continuous Hamiltonian respects a Π_C symmetry, i.e., $\Pi_C H_{2D} \Pi_C^{-1} = H_{2D}$, where $\Pi_C = M\sigma_x S_4^{-1}$ with $M H_{2D}(x, y) M^{-1} = H_{2D}(y, x)$; the representation of this symmetry in the momentum space corresponds to $\Pi H_{TB}^{2D}(\mathbf{k}) \Pi^{-1} = H_{TB}^{2D}(k_y, k_x)$ [$H_{TB}^{2D} \equiv H_{TB}(h_z = 0)$] with $\Pi = (\sigma_x - \sigma_y)/\sqrt{2}$, indicating that the additional term must take the form of $\sigma_x - \sigma_y$. In Fig. 5(b1-b2), we plot the spectra of the continuous and tight-binding models and both figures illustrate that a four-fold degenerate touching point splits into two doubly degenerate ones. Our further comparison around a touching point in Fig. 5(b3-b4) shows the quantitative agreement of the latter with the former.

Appendix B: ANALYSIS OF MANY-BODY EFFECTS

In this section, we make a crude estimate of many-body effects on the degenerate points in the presence of weak repulsive atom-atom interactions for fermionic atoms. For alkali atoms, the interaction readily tuned by Feshbach resonances is short-range and can be written as

(we only consider dominant on-site interactions)

$$H_{Int} = g \sum_{k_z k'_z Q} \sum_{\mathbf{x}} \hat{c}_{k_z \mathbf{x} \uparrow}^\dagger \hat{c}_{-k_z + Q \mathbf{x} \downarrow} \hat{c}_{-k'_z + Q \mathbf{x} \downarrow} \hat{c}_{k'_z \mathbf{x} \uparrow}, \quad (\text{A15})$$

where g denotes the strength of interactions proportional to the s -wave scattering length. For weak interactions, using mean-field approximations yields

$$H_{Int} \approx \sum_{\mathbf{k}} \Psi(\mathbf{k})^\dagger H_{Int}^M(\mathbf{k}) \Psi(\mathbf{k}) + N \sum_{D=A,B} \frac{|m_{\parallel,D}|^2}{g} - N \sum_{D=A,B} \frac{m_{z,\uparrow,D} m_{z,\downarrow,D}}{g}, \quad (\text{A16})$$

where N is the number of sites in the (x, y) plane,

$$m_{z,\sigma,D} = g \sum_{k_z} \langle \hat{D}_{k_z \mathbf{x} \sigma}^\dagger \hat{D}_{k_z \mathbf{x} \sigma} \rangle, \quad (\text{A17})$$

$$\begin{aligned} m_{\parallel,D} &= m_{x,D} + i m_{y,D} \\ &= g \sum_{k_z} \langle \hat{D}_{k_z \mathbf{x}, \uparrow}^\dagger \hat{D}_{k_z \mathbf{x}, \downarrow} \rangle \end{aligned} \quad (\text{A18})$$

and

$$H_{Int}^M(\mathbf{k}) = m_{z,1} + m_{z,2} \sigma_z + m_{x,1} \sigma_x + m_{y,1} \sigma_y + m_{z,3} \tau_z + m_{z,4} \sigma_z \tau_z + m_{x,2} \sigma_x \tau_z + m_{y,2} \sigma_y \tau_z, \quad (\text{A19})$$

with

$$m_{z,1} = \frac{1}{4} (m_{z,\downarrow,A} + m_{z,\uparrow,A} + m_{z,\downarrow,B} + m_{z,\uparrow,B}), \quad (\text{A20})$$

$$m_{z,2} = \frac{1}{4} (m_{z,\downarrow,A} - m_{z,\uparrow,A} + m_{z,\downarrow,B} - m_{z,\uparrow,B}), \quad (\text{A21})$$

$$m_{z,3} = \frac{1}{4} (m_{z,\downarrow,A} + m_{z,\uparrow,A} - m_{z,\downarrow,B} - m_{z,\uparrow,B}), \quad (\text{A22})$$

$$m_{z,4} = \frac{1}{4} (m_{z,\downarrow,A} - m_{z,\uparrow,A} - m_{z,\downarrow,B} + m_{z,\uparrow,B}), \quad (\text{A23})$$

and

$$m_{x,1} = -\frac{1}{2} (m_{x,A} + m_{x,B}), \quad (\text{A24})$$

$$m_{x,2} = -\frac{1}{2} (m_{x,A} - m_{x,B}), \quad (\text{A25})$$

$$m_{y,1} = -\frac{1}{2} (m_{y,A} + m_{y,B}), \quad (\text{A26})$$

$$m_{y,2} = -\frac{1}{2} (m_{y,A} - m_{y,B}). \quad (\text{A27})$$

If we consider using the ground state of non-interacting fermionic atoms as the initial state for iteration while searching for the many-body ground state, we have $m_{z,\sigma,A} = m_{z,\sigma,B}$ and $m_{x,A} = m_{x,B} = m_{y,A} = m_{y,B} = 0$, so that $m_{z,3} = m_{z,4} = m_{x,1} = m_{y,1} = m_{x,2} = m_{y,2} = 0$. Based on this argument, we have

$$H_{Int}(\mathbf{k}) = m_{z,1} + m_{z,2} \sigma_z. \quad (\text{A28})$$

Clearly, the presence of interactions may induce an effective Zeeman field, which will shift the locations of degenerate points along the z direction and may cause the transition between the type-I and type-II, but will neither destroy Weyl nor four-fold degenerate points.

-
- [1] I. M. Lifshitz, Anomalies of electron characteristics of a metal in the high pressure region, *Sov. Phys. JETP* **11**, 1130 (1960).
- [2] G. E. Volovik, *The Universe in a Helium Droplet* (Clarendon Press, Oxford, 2003).
- [3] S. Murakami, Phase transition between the quantum spin Hall and insulator phases in 3D: emergence of a topological gapless phase, *New Journal of Physics* **9**, 356 (2007).
- [4] X. Wan, A. M. Turner, A. Vishwanath, and S. Y. Savrasov, Topological semimetal and Fermi-arc surface states in the electronic structure of pyrochlore iridates, *Phys. Rev. B* **83**, 205101 (2011).
- [5] O. Vafek and A. Vishwanath, Dirac Fermions in Solids: From High-Tc Cuprates and Graphene to Topological Insulators and Weyl Semimetals, *Annual Review of Condensed Matter Physics* **5**, 83 (2014).
- [6] A. A. Soluyanov, D. Gresch, Z. Wang, Q. Wu, M. Troyer, X. Dai, and B. A. Bernevig, Type-II Weyl semimetals, *Nature* **527**, 495 (2015).
- [7] Y. Xu, F. Zhang, and C. Zhang, Structured Weyl Points in Spin-Orbit Coupled Fermionic Superfluids, *Phys. Rev. Lett.* **115**, 265304 (2015).
- [8] H. Weyl, *Zeitschrift für Physik* **56**, 330 (1929).
- [9] E. J. Bergholtz, Z. Liu, M. Trescher, R. Moessner, and M. Udagawa, Topology and Interactions in a Frustrated Slab: Tuning from Weyl Semimetals to $C > 1$ Fractional Chern Insulators, *Phys. Rev. Lett.* **114**, 016806 (2015).
- [10] Z. Yu, Y. Yao, and S. A. Yang, Unusual Magneto-Response in Type-II Weyl Semimetals, arXiv:1604.04030.
- [11] M. Udagawa and E. J. Bergholtz, Field-Selective Anomalous and Chiral Charge Reversal in Type-II Weyl Materials, arXiv:1604.08457.
- [12] G.E. Volovik, Lifshitz transitions via the type-II Dirac and type-II Weyl points, arXiv:1604.00849.
- [13] A. A. Zyuzin and R. P. Tiwari, Intrinsic Anomalous Hall Effect in Type-II Weyl Semimetals, arXiv:1601.00890.

- [14] T. E. O'Brien, M. Diez, and C. W. J. Beenakker, Magnetic breakdown and Klein tunneling in a type-II Weyl semimetal, *Phys. Rev. Lett.* **116**, 236401 (2016).
- [15] Z. Wang, D. Gresch, A. A. Soluyanov, W. Xie, S. Kushwaha, X. Dai, M. Troyer, R. J. Cava, and B. A. Bernevig, MoTe₂: Weyl and Line Node Topological Metal, arXiv:1511.07440.
- [16] T.-R. Chang, S.-Y. Xu, G. Chang, C.-C. Lee, S.-M. Huang, B. Wang, G. Bian, H. Zheng, D. S. Sanchez, I. Belopolski, N. Alidoust, M. Neupane, A. Bansil, H.-T. Jeng, H. Lin, and M. Zahid Hasan, Prediction of an arc-tunable Weyl Fermion metallic state in MoxW_{1-x}Te₂, *Nat. Commun.* **7**, 10639 (2016).
- [17] K. Koepnik, D. Kasinathan, D. V. Efremov, S. Khim, S. Borisenko, B. Büchner, and J. van den Brink, TaIrTe₄ a ternary Type-II Weyl semi-metal, arXiv:1603.04323.
- [18] J. Liu, H. Wang, C. Fang, L. Fu, and X. Qian, Van der Waals Stacking Induced Topological Phase Transition in Layered Ternary Transition Metal Chalcogenides, arXiv:1605.03903.
- [19] L. Huang, T. M. McCormick, M. Ochi, Z. Zhao, M. Suzuki, R. Arita, Y. Wu, D. Mou, H. Cao, J. Yan, N. Trivedi, and A. Kaminski, Spectroscopic evidence for type II Weyl semimetal state in MoTe₂, arXiv:1603.06482.
- [20] S.-Y. Xu, N. Alidoust, G. Chang, H. Lu, B. Singh, I. Belopolski, D. Sanchez, X. Zhang, G. Bian, H. Zheng, M.-A. Hsuan, Y. Bian, S.-M. Huang, C.-H. Hsu, T.-R. Chang, H.-T. Jeng, A. Bansil, V. N. Strocov, H. Lin, S. Jia, and M. Z. Hasan, Discovery of Lorentz-violating Weyl fermion semimetal state in LaAlGe materials, arXiv:1603.07318.
- [21] K. Deng, G. Wan, P. Deng, K. Zhang, S. Ding, E. Wang, M. Yan, H. Huang, H. Zhang, Z. Xu, J. Denlinger, A. Fedorov, H. Yang, W. Duan, H. Yao, Y. Wu, S. Fan, H. Zhang, X. Chen, and S. Zhou, Experimental observation of topological Fermi arcs in type-II Weyl semimetal MoTe₂, arXiv:1603.08508.
- [22] J. Jiang, Z. K. Liu, Y. Sun, H. F. Yang, R. Rajamathi, Y. P. Qi, L. X. Yang, C. Chen, H. Peng, C.-C. Hwang, S. Z. Sun, S.-K. Mo, I. Vobornik, J. Fujii, S. S. P. Parkin, C. Felser, B. H. Yan, and Y. L. Chen, Observation of the Type-II Weyl Semimetal Phase in MoTe₂, arXiv:1604.00139.
- [23] A. Liang, J. Huang, S. Nie, Y. Ding, Q. Gao, C. Hu, S. He, Y. Zhang, C. Wang, B. Shen, J. Liu, P. Ai, L. Yu, X. Sun, W. Zhao, S. Lv, D. Liu, C. Li, Y. Zhang, Y. Hu, Y. Xu, L. Zhao, G. Liu, Z. Mao, X. Jia, F. Zhang, S. Zhang, F. Yang, Z. Wang, Q. Peng, H. Weng, X. Dai, Z. Fang, Z. Xu, C. Chen, and X. J. Zhou, Electronic Evidence for Type II Weyl Semimetal State in MoTe₂, arXiv:1604.01706.
- [24] N. Xu, Z. J. Wang, A. P. Weber, A. Magrez, P. Bugnon, H. Berger, C. E. Matt, J. Z. Ma, B. B. Fu, B. Q. Lv, N. C. Plumb, M. Radovic, E. Pomjakushina, K. Conder, T. Qian, J. H. Dil, J. Mesot, H. Ding, and M. Shi, Discovery of Weyl semimetal state violating Lorentz invariance in MoTe₂, arXiv:1604.02116.
- [25] F. Y. Bruno, A. Tamai, Q. S. Wu, I. Cucchi, C. Barreteau, A. de la Torre, S. McKeown Walker, S. Riccò, Z. Wang, T. K. Kim, M. Hoesch, M. Shi, N. C. Plumb, E. Giannini, A. A. Soluyanov, and F. Baumberger, Surface states and bulk electronic structure in the candidate type-II Weyl semimetal WTe₂, arXiv:1604.02411.
- [26] Y. -J. Lin, K. Jiménez-García, and I. B. Spielman, Spin-orbit-coupled Bose-Einstein condensates, *Nature (London)* **471**, 83 (2011).
- [27] J. -Y. Zhang, S. -C. Ji, Z. Chen, L. Zhang, Z. -D. Du, B. Yan, G. -S. Pan, B. Zhao, Y. -J. Deng, H. Zhai, S. Chen, and J. -W. Pan, Collective Dipole Oscillations of a Spin-Orbit Coupled Bose-Einstein Condensate, *Phys. Rev. Lett.* **109**, 115301 (2012).
- [28] P. Wang, Z. -Q. Yu, Z. Fu, J. Miao, L. Huang, S. Chai, H. Zhai, and J. Zhang, Spin-Orbit Coupled Degenerate Fermi Gases, *Phys. Rev. Lett.* **109**, 095301 (2012).
- [29] L. W. Cheuk, A. T. Sommer, Z. Hadzibabic, T. Yefsah, W. S. Bakr, and M. W. Zwierlein, Spin-Injection Spectroscopy of a Spin-Orbit Coupled Fermi Gas, *Phys. Rev. Lett.* **109**, 095302 (2012).
- [30] C. Qu, C. Hamner, M. Gong, C. Zhang, and P. Engels, Observation of Zitterbewegung in a spin-orbit-coupled Bose-Einstein condensate, *Phys. Rev. A* **88**, 021604(R) (2013).
- [31] L. Huang, Z. Meng, P. Wang, P. Peng, S.-L. Zhang, L. Chen, D. Li, Q. Zhou, and J. Zhang, Experimental realization of a two-dimensional synthetic spin-orbit coupling in ultracold Fermi gases, *Nat. Phys.* **12**, 540 (2016).
- [32] Z. Meng, L. Huang, P. Peng, D. Li, L. Chen, Y. Xu, C. Zhang, P. Wang, and J. Zhang, Experimental observation of topological band gap opening in ultracold Fermi gases with two-dimensional spin-orbit coupling, arXiv:1511.08492.
- [33] Z. Wu, L. Zhang, W. Sun, X.-T. Xu, B.-Z. Wang, S.-C. Ji, Y. Deng, S. Chen, X.-J. Liu, and J.-W. Pan, Realization of Two-Dimensional Spin-orbit Coupling for Bose-Einstein Condensates, *Science* **354**, 83 (2016).
- [34] N. Q. Burdick, Y. Tang, and B. L. Lev, A long-lived spin-orbit-coupled dipolar Fermi gas, arXiv:1605.03211.
- [35] J. Li, W. Huang, B. Shteynas, S. Burchesky, F. C. Top, E. Su, J. Lee, A. O. Jamison, and W. Ketterle, Spin-Orbit Coupling and Spin Textures in Optical Superlattices, arXiv:1606.03514.
- [36] I. Bloch, J. Dalibard, and S. Nascimbene, Quantum simulations with ultracold quantum gases, *Nat. Phys.* **8**, 267 (2012).
- [37] V. Galitski and I. B. Spielman, Spin-orbit coupling in atomic gases, *Nature* **495**, 49 (2013).
- [38] N. Goldman, J. C. Budich, and P. Zoller, Topological quantum matter with ultracold gases in optical lattices, *Nat. Phys.* **12**, 639 (2016).
- [39] M. Gong, S. Tewari, and C. Zhang, BCS-BEC Crossover and Topological Phase Transition in 3D Spin-Orbit Coupled Degenerate Fermi Gases, *Phys. Rev. Lett.* **107**, 195303 (2011).
- [40] K. Seo, C. Zhang, and S. Tewari, Thermodynamic signatures for topological phase transitions to Majorana and Weyl superfluids in ultracold Fermi gases, *Phys. Rev. A* **87**, 063618 (2013).
- [41] Y. Xu, R.-L. Chu, and C. Zhang, Anisotropic Weyl Fermions from the Quasiparticle Excitation Spectrum of a 3D Fulde-Ferrell Superfluid, *Phys. Rev. Lett.* **112**, 136402, (2014).
- [42] H. Hu, L. Dong, Y. Cao, H. Pu, and X.-J. Liu, Gapless topological Fulde-Ferrell superfluidity induced by an in-plane Zeeman field, *Phys. Rev. A* **90**, 033624 (2014).
- [43] Y. Xu and C. Zhang, Topological Fulde-Ferrell superfluids of a spin-orbit coupled Fermi gas, *Int. J. Mod. Phys. B* **29**, 1530001 (2015).

- [44] B. M. Anderson, G. Juzeliunas, V. M. Galitski, and I. B. Spielman, Synthetic 3D Spin-Orbit Coupling, *Phys. Rev. Lett.* **108**, 235301 (2012).
- [45] J. H. Jiang, Tunable topological Weyl semimetal from simple-cubic lattices with staggered fluxes, *Phys. Rev. A* **85**, 033640 (2012).
- [46] S. Ganeshan, and S. Das Sarma, Constructing a Weyl semimetal by stacking one dimensional topological phases, *Phys. Rev. B* **91**, 125438 (2015).
- [47] T. Dubček, C. J. Kennedy, L. Lu, W. Ketterle, M. Soljačić, and Hrvoje Buljan, Weyl points in three-dimensional optical lattices: synthetic magnetic monopoles in momentum space, *Phys. Rev. Lett.* **114**, 225301 (2015).
- [48] W.-Y. He, S. Zhang, and K. T. Law, The realization and detection of Weyl semimetals in cold atomic systems, arXiv:1501.02348.
- [49] X.-L. Qi, T. L. Hughes, and S.-C. Zhang, Topological field theory of time-reversal invariant insulators, *Phys. Rev. B* **78**, 195424 (2008).
- [50] H. Shapourian and T. L. Hughes, Phase diagrams of disordered Weyl semimetals, *Phys. Rev. B* **93**, 075108 (2016).
- [51] Y. Chen, Y. Xie, S. A. Yang, H. Pan, F. Zhang, M. L. Cohen, and S. Zhang, Spin-orbit-free Weyl-loop and Weyl-point semimetals in a stable three-dimensional carbon allotrope, *Nano Lett.* **15**, 6974 (2015).
- [52] D. Xiao, M.-C. Chang, and Q. Niu, Berry phase effects on electronic properties, *Rev. Mod. Phys.* **82**, 1959 (2010).
- [53] X.-J. Liu, K. T. Law, and T. K. Ng, Realization of 2D Spin-Orbit Interaction and Exotic Topological Orders in Cold Atoms, *Phys. Rev. Lett.* **112**, 086401 (2014).
- [54] Y. Xu and C. Zhang, Dirac and Weyl rings in three-dimensional cold-atom optical lattices, *Phys. Rev. A* **93**, 063606 (2016).
- [55] L. Tarruell, D. Greif, T. Uehlinger, G. Jotzu, and T. Esslinger, Creating, moving and merging Dirac points with a Fermi gas in a tunable honeycomb lattice, *Nature (London)* **483**, 302 (2012).
- [56] L.-K. Lim, J.-N. Fuchs, and G. Montambaux, Bloch-Zener Oscillations across a Merging Transition of Dirac Points, *Phys. Rev. Lett.* **108**, 175303 (2012).
- [57] Y.-Q. Wang and X.-J. Liu, A Scaling Behavior of Bloch Oscillation in Weyl Semimetals, arXiv:1605.02671.
- [58] L. D. Landau, *Phys. Z. Sowjetunion* **2**, 46 (1932); C. Zener, *Proc. R. Soc. A* **137**, 696 (1932).